PCCP

PAPER

View Article Online
View Journal | View Issue

Cite this: *Phys. Chem. Chem. Phys.*, 2019, **21**, 21824

Structure, electrical conductivity and oxygen transport properties of perovskite-type oxides $CaMn_{1-x-y}Ti_xFe_yO_{3-\delta}$†

Rian Ruhl,[a] Jia Song,[a] Vincent Thoréton,*[b] Sathya Prakash Singh,[b] Kjell Wiik,[b] Yngve Larring[c] and Henny J. M. Bouwmeester*[a]

Received 4th September 2019,
Accepted 18th September 2019

DOI: 10.1039/c9cp04911h

rsc.li/pccp

Calcium manganite-based perovskite-type oxides hold promise for application in chemical looping combustion processes and oxygen transport membranes. In this study, we have investigated the structure, electrical conductivity and oxygen transport properties of perovskite-type oxides $CaMn_{1-x-y}Ti_xFe_yO_{3-\delta}$. Distinct from previous work, data of high-temperature X-ray diffraction (HT-XRD) in the temperature range 600–1000 °C (with intervals of 25 °C) demonstrates that $CaMnO_{3-\delta}$ (CM) transforms from orthorhombic to a mixture of orthorhombic and tetragonal phases between 875 °C and 900 °C. Rietveld refinements show the formation of a pure tetragonal phase at 975 °C and of a pure cubic phase at 1000 °C. Partial substitution of manganese by iron and/or titanium to yield $CaMn_{0.875}Ti_{0.125}O_{3-\delta}$ (CMT), $CaMn_{0.85}Fe_{0.15}O_{3-\delta}$ (CMF) or $CaMn_{0.725}Ti_{0.125}Fe_{0.15}O_{3-\delta}$ (CMTF) leads to different phase behaviours. While CMT remains orthorhombic up to the highest temperature covered by the HT-XRD experiments, CMF and CMTF undergo an orthorhombic → tetragonal → cubic sequence of phase transitions. Electrical conductivity relaxation measurements are conducted to determine the chemical diffusion coefficient (D_{chem}) and the surface exchange coefficient (k_{chem}) of the materials. The results demonstrate that oxygen transport is hindered in the tetragonal phase, when occurring, which is attributed to a possible ordering of oxygen vacancies. The small polaron electrical conductivity of CM in the cited temperature range is lowered upon partial manganese substitution, by about 10% for CMF and up to half an order of magnitude for CMT and CMTF.

1. Introduction

Chemical looping combustion (CLC) is a combustion technology for power and heat generation integrated with CO_2 capture.[1–6] The gaseous fuel is oxidized by lattice oxygen from a solid oxide, typically a transition metal-containing oxide. The oxygen carrier material (OCM) is circulated between the fuel reactor and an adjacent air reactor, where it is re-oxidized by air for the next cycle. The combustion reaction produces CO_2 and H_2O, which can easily be separated by condensation, hence producing a pure CO_2 stream. CLC technology is conceptually linked to membrane-based oxyfuel combustion, where oxygen is supplied to the fuel by an oxygen transport membrane (OTM), separating oxygen from air.[7–10] Both applications rely on solid oxides (referring to the OCM and OTM materials), showing fast oxygen transport kinetics and reliable operation in atmospheres containing CO_2, SO_2, and/or water.

Calcium manganite, in which 12.5 mol% of manganese is substituted by titanium, was shown to hold promise for CLC applications.[11–13] Recently, we demonstrated an improved performance for $CaMn_{0.875-x}Ti_{0.125}Fe_xO_{3-\delta}$.[14] The partial co-substitution of manganese by titanium and iron enhances both the oxygen storage capacity and release kinetics and lowers the degradation rate. Optimal performance was found for the composition with 15 mol% iron.[14] Asymmetric OTM membranes based on $CaMn_{0.25}Ti_{0.6}Fe_{0.15}O_{3-\delta}$ operated in CO_2-containing atmospheres showed a stable oxygen flux over 6 months, without significant degradation.[15] In the present study, we have determined the evolution of structure and oxygen transport properties of $CaMnO_{3-\delta}$ (CM), $CaMn_{0.875}Ti_{0.125}O_{3-\delta}$ (CMT), $CaMn_{0.85}Fe_{0.15}O_{3-\delta}$ (CMF), and $CaMn_{0.725}Ti_{0.125}Fe_{0.15}O_{3-\delta}$ (CMTF) with temperature, using high-temperature X-ray diffraction, differential thermal analysis, thermogravimetry and electrical conductivity relaxation measurements.

[a] *Electrochemistry Research Group, Membrane Science and Technology, MESA+ Institute for Nanotechnology, Faculty of Science and Technology, University of Twente, P.O. Box 217, 7500 AE, Enschede, The Netherlands. E-mail: h.j.m.bouwmeester@utwente.nl*
[b] *Department of Materials Science and Engineering, Norwegian University of Science and Technology (NTNU), NO-7491 Trondheim, Norway. E-mail: vincent.thoreton@smn.uio.no*
[c] *SINTEF Industry, Sustainable Energy Technology, P.O. Box 124, Blindern, 0314 Oslo, Norway*

† Electronic supplementary information (ESI) available. See DOI: 10.1039/c9cp04911h

2. Experimental

2.1 Powder synthesis and sintering

Powders of CM, CMT, CMF and CMTF were synthesized as described elsewhere.[4] The powders were milled in ethanol for 30 min using a planetary ball mill (Retsch PM 100) with a 150 mm diameter zirconia bowl and 5 mm zirconia balls operated at 250 rpm. The powder was dried and sieved, and the fraction below 45 μm was uniaxially pressed into a pellet, which was further compacted using a cold isostatic press at 400 MPa. Further densification was achieved by the following procedure: the green pellet was placed onto a platinum foil inside a tubular furnace and heated (200 K h^{-1}) under a flow of 2% H_2 in nitrogen up to ~800 °C. Upon reaching that temperature, the atmosphere was changed to a flow of pure nitrogen, and the sample further heated with an unchanged rate until the sintering temperature was reached (1450 °C for CM and CMT, 1400 °C for CMF and CMTF), followed by a dwell of 12 h at this temperature.[16] Subsequently, the sample was cooled at a rate of 5 °C min^{-1} to 1250 °C, at which the gas flow was changed to 10% oxygen in nitrogen. The sample was kept for 6 h at the temperature of 1250 °C, and subsequently slowly cooled down at 1 °C min^{-1} to room temperature to avoid the formation of cracks. Dense ceramic pellets were obtained with relative densities in excess of 99%, as measured by Archimedes' method.

2.2 X-ray diffraction

Room temperature powder X-ray diffraction (XRD) measurements were performed on a Rigaku SmartLab X-Ray Diffractometer in Bragg–Brentano mode (Cu Kα radiation). Finely ground and sieved powder (<90 μm) was dispersed onto the sample holder and data was collected from 15 to 60° with a step size of 0.02° and 0.5° per minute min scanning speed. For high-temperature X-ray diffraction measurements (HT-XRD) measurements, a Rigaku Ultima IV instrument with CuKα radiation accelerated at 40 kV and 40 mA was employed. The powder samples were heated to 975 °C under a 30 ml min^{-1} flow of synthetic air. XRD patterns were recorded from 975 °C or 1000 °C down to 600 °C with 25 °C intervals. At each temperature the sample was allowed to equilibrate for 10 min. Data were acquired in the 2θ range 10–75° with a step size of 0.02° and a scan speed of 1 °C min^{-1}. The Full Prof software package was used for Rietveld refinements of the obtained patterns.[17] Room temperature XRD patterns of sintered ceramic bodies were recorded on a Bruker D2 Phaser instrument with Cu-Kα radiation (λ = 1.54184 Å).

2.3 Thermal analysis

Differential thermal analysis (DTA) and thermogravimetric analysis (TGA) data were collected on a Netzsch STA 449 F3 Jupiter instrument. Prior to experiments, the samples held in alumina crucibles were heated to 1000 °C under a synthetic air flow to remove any adsorbed species. After a dwell of 30 min at this temperature, the sample was cooled to 100 °C. For DTA experiments, about 50 mg of powder was used. Measurements were performed in the range 100–1000 °C, with heating and cooling rates of 10 °C min^{-1}. Data were corrected for the instrumental background obtained by recording data for an empty crucible under the same conditions. Throughout the experiments, the flow rate was kept constant at 100 ml min^{-1}.

For determining accurately changes in the oxygen stoichiometry of the samples, TGA experiments were conducted using about 175 mg of powder. Data were collected during cooling from 1000 to 650 °C, with intervals of 25 °C, at 4.5, 10, 21, 42 and 90% O_2 in N_2, maintaining a total flow rate of 200 ml min^{-1} (STP). Heating and cooling rates were set at 10 °C min^{-1}. The chosen partial pressures of oxygen correspond with those used in the electrical conductivity relaxation (ECR) experiments. At each temperature and oxygen partial pressure, the sample was allowed to equilibrate. Dwell stages were 30 min in the range 1000–775 °C, 45 min at 750 and 725 °C, 60 min at 700 and 675 °C, and 90 min at 650 °C. The measured mass was corrected for the buoyancy effect by subtracting the data for an empty crucible under the same conditions.

2.4 Electrical conductivity and conductivity relaxation measurements

Thin rectangular bars with approximate dimensions 12 × 6 × 0.5 mm^3 were cut out of the sintered sample pellets, and the two largest surfaces polished until a mirror-like finish was obtained. The final thicknesses of the samples were 0.64 mm, 0.57 mm, 0.47 mm and 0.46 mm for CM, CMT, CMF, and CMTF, respectively. A four-probe dc method was used to collect data on electrical conductivity. To this end two gold wires (Alfa Aesar, 99.999%, 0.25 mm in diameter and approximately 4 cm in length) were wrapped around the sample close to the bar ends to serve as current leads. Two additional gold wires were wrapped around the sample, about 2 mm remote from the previously fixed electrodes, as voltage probes. Prior to mounting, four indents were cut using a diamond blade along each long side of the sample for fixing of the electrodes. Sulphur-free gold paste (MaTeck GmbH, Jülich, Germany) was applied to improve electrical contact between electrodes and sample. Finally, the sample was thermally treated in air to sinter the gold paste, using a chamber furnace at a temperature of 950 °C. Heating and cooling rates throughout the experiments were set at 1 °C min^{-1}.

The sample was suspended above an alumina rod functioning as the sample holder by tightly wrapping the sample electrodes around the Au wires of the sample holder. Care was taken that gas could flow freely around the sample. The sample holder was slid into the Al_2O_3 reactor with a diameter of 12 mm, thereby confining the sample to a chamber with a volume of 2.58 cm^3. Using a gas flow rate of 280 ml min^{-1} and assuming a continuously ideally stirred tank reactor, the small reactor volume ensures a flush time between 0.13 s at 925 °C and 0.16 s at 650 °C. A K-type thermocouple was placed a few millimetres beneath the sample and used to continuously monitor the temperature. Two parallel gas streams, each with a total flow rate of 280 ml min^{-1}, with different pO_2 values (between 0.01 and 1 atm) were created by mixing dried oxygen and nitrogen in the desired

ratios using Brooks GF040 mass flow controllers. One of the streams was led through the reactor and, subsequently, through an oxygen sensor (Systech Zr893/4). A pneumatically-operated four-way valve was utilised to rapidly switch between both gas streams to achieve an instantaneous change in pO_2. A Keithley 2400 SourceMeter® was used to provide a current of 30–100 mA through the sample, the magnitude depending on the sample conductivity. Another instrument of the same type was used to measure the voltage over the sample with a sampling rate of about 10 Hz.

The sample was heated to 925 °C under a 280 ml min^{-1} flow of synthetic air (pO_2 = 0.21 atm). Electrical conductivity relaxation (ECR) measurements were performed after step changes in pO_2 between 0.147 to 0.215 atm. It was assumed that equilibrium was reached after a time of $15\tau_c$, where τ_c is the characteristic time when the transient conductivity is fitted to a regular exponential function of the elapsed time. A series of five oxidation and reduction steps was performed for each temperature in the range 925–650 °C. The temperature was changed stepwise, with intervals of 25 °C. To check the reproducibility, the same series of oxidation and reduction steps was repeated by increasing the temperature back to 925 °C and measuring again at each 25 °C interval. The series of measurements was set up with a custom-made LabVIEW program, which was also used for data acquisition. Data on the electrical conductivity of the samples was collected at each temperature.

The transient conductivity after each pO_2 step change was normalized according to eqn (1). Normalized data were cut off at $10\tau_c$ and fitted to eqn (2)–(4) to obtain the chemical diffusion coefficient D_{chem} and the surface exchange coefficient k_{chem}.

$$g(t) = \frac{\sigma(t) - \sigma_0}{\sigma_\infty - \sigma_0} \tag{1}$$

$$g(t) = 1 - \prod_{i=y,z} \sum_{m=1}^{\infty} \frac{2L_i^2}{\beta_{m,i}^2\left(\beta_{m,i}^2 + L_i^2 + L_i\right)} \frac{\tau_{m,i}}{\tau_{m,i} - \tau_f} \times \left(e^{-\frac{t}{\tau_{m,i}}} - \frac{\tau_f}{\tau_{m,i}}\left(e^{-\frac{t}{\tau_f}}\right)\right) \tag{2}$$

$$\tau_{m,i} = \frac{b_i^2}{D_{chem}\beta_{m,i}^2} \tag{3}$$

$$L_i = \frac{b_i}{L_c} = \beta_{m,i} \tan \beta_{m,i} \tag{4}$$

In these equations, $g(t)$ is the normalized conductivity, σ_0 and σ_∞ are the conductivities $\sigma(t)$ at time t = 0 and t = ∞, respectively, τ_f the flush time constant of the reactor, and $2b_i$ the sample dimension along coordinate i, whilst $\beta_{m,i}$ are the non-zero roots of eqn (4). The critical thickness $L_c = D_{chem}/k_{chem}$ is the critical thickness below which oxygen surface exchange prevails over bulk oxygen diffusion in determining the rate of re-equilibration rate after a pO_2 step change. The flush time τ_f was calculated from

$$\tau_f = \frac{V_r}{\theta_v}\frac{T_{STP}}{T_r} \tag{5}$$

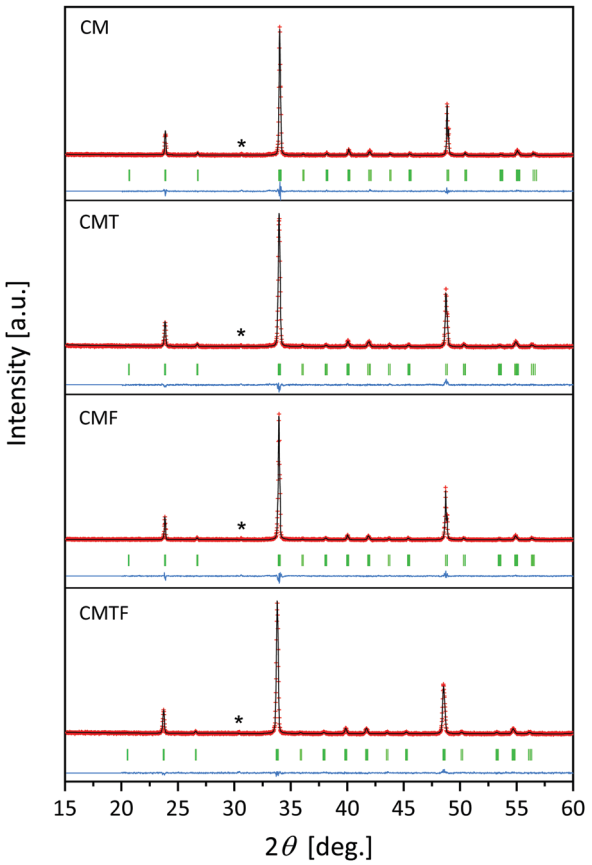

Fig. 1 Measured (red symbols) and calculated (black line) XRD patterns for CM, CMT, CMF and CMTF at room temperature. Bragg positions and the residual plot are indicated. Extra peaks attributed to copper Kβ are labelled with a star (*).

in which V_r is the volume (2.58 cm^3) of the chamber in which the sample is located, θ_v the gas flow rate through the reactor, T_r the temperature in the reactor, and T_{STP} the temperature at standard conditions. D_{chem} and k_{chem}, together with t_0, were fitted using a non-linear least-squares program based on the Levenberg–Marquardt algorithm. To prevent finding local minima in the fitting routine, initial estimates for the fitting parameters were calculated, using

$$D_{init} \approx \frac{b_z^2}{\tau_c} \tag{6}$$

$$k_{init} \approx \frac{b_z}{\tau_c} \tag{7}$$

where D_{init} and k_{init} are the initial values for the fitting parameters D_{chem} and k_{chem}, respectively, and b_z is half the sample thickness, noting that $b_z \ll b_x, b_y$. Eqn (6) assumes that diffusion governs the relaxation, while eqn (7) assumes that surface exchange governs the relaxation. The intersection between the tangent line of the conductivity before the pO_2 step and that of the conductivities between g = 0.005 and g = 0.05 served as the initial value for the parameter t_0. Values of D_{chem} and k_{chem} obtained from fitting data of at least three

Table 1 Structural parameters and reliability factors obtained from Rietveld refinements of room temperature XRD patterns. The numbers in parentheses denote standard deviations in units of the least significant digits

	a [Å]	b [Å]	c [Å]	V [Å^3]	R_{Bragg} [%]	R_{wp} [%]	χ^2 [–]
CM	5.2803(2)	7.4527(3)	5.2639(2)	207.154(2)	3.382	14.62	1.42
CMT	5.2965(5)	7.4754(9)	5.2779(5)	208.982(4)	4.972	16.90	1.25
CMF	5.2964(1)	7.4778(2)	5.2835(1)	209.263(1)	5.878	15.20	1.51
CMTF	5.3138(7)	7.4970(6)	5.3002(5)	211.154(4)	3.709	15.30	1.14

subsequent reduction steps were averaged. Additional descriptions of the ECR technique and the model used for data fitting are given elsewhere.[18,19]

3. Results and discussion

3.1 Structure and phase stability

Room temperature XRD powder diffractograms of CM, CMT, CMF and CMTF are shown in Fig. 1. The corresponding structural parameters and reliability factors obtained from Rietveld refinements in the orthorhombic space group *Pnma* are listed in Table 1. Analysis reveals that all four compositions are single phase. The cell parameters obtained for CM are found to be in good agreement with a = 5.281(1) Å, b = 7.453(1) Å and c = 5.266(1) Å reported by Leonidova *et al.*,[20] a = 5.274(3) Å, b = 7.467(5) Å and c = 5.277(2) Å by Rørmark *et al.*,[21] and a = 5.282 Å, b = 7.452 Å and c = 5.265 Å by Taguchi *et al.*[22] The small differences between the obtained data in each of these studies and the current study might be related to a different oxygen stoichiometry of the samples, depending on the atmosphere and cooling rate. Analysis of the room temperature XRD patterns of sintered ceramic bodies of CM, CMT, CMF and CMTF revealed no apparent differences with those of the corresponding powders displayed in Fig. 1.

Fig. S1 (ESI†) shows the HT-XRD patterns of CM recorded in air on cooling from 1000 °C to 600 °C. On the basis of a combined DTA and HT-XRD (at room temperature, 900 °C and 920 °C) study, Taguchi *et al.*[22] proposed a phase transition sequence for CM from orthorhombic (*Pnma*) to tetragonal (*I*4/*mcm*) at 896 °C, and

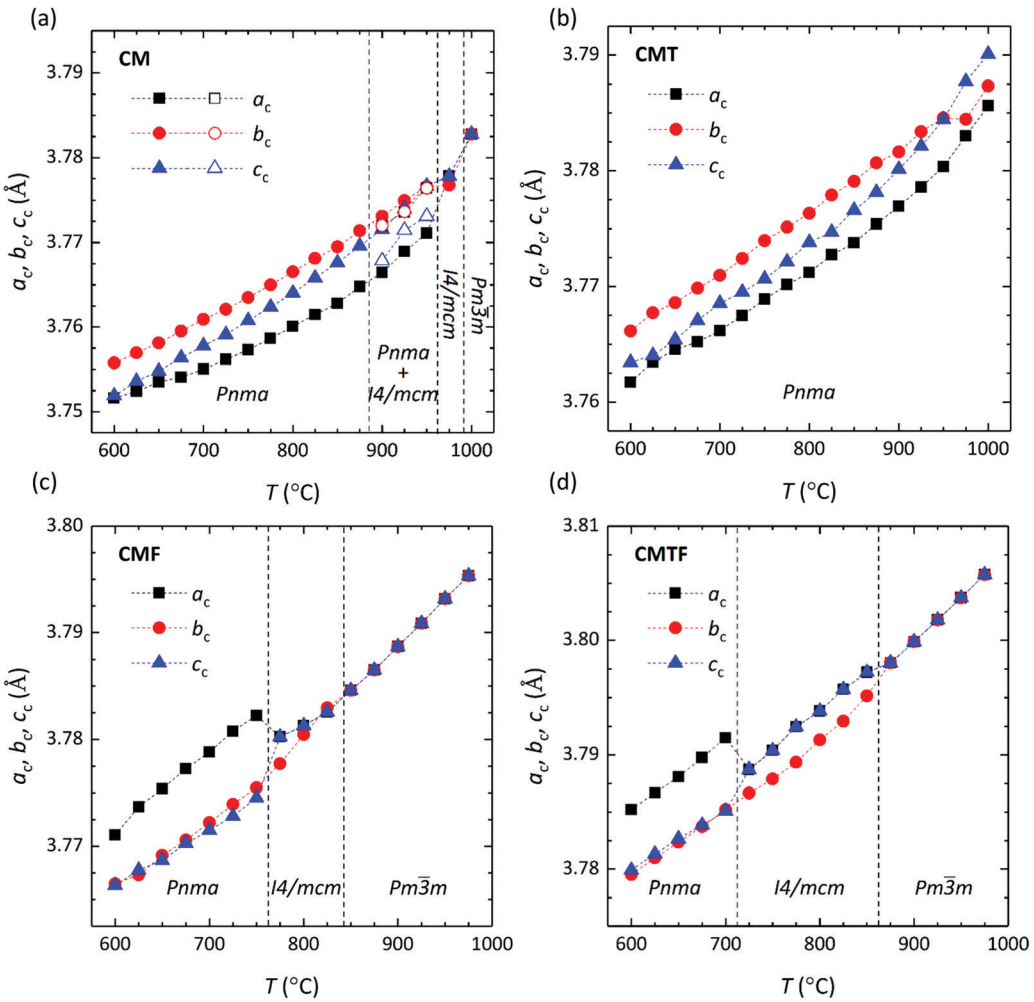

Fig. 2 Pseudo cubic lattice parameters as a function of temperature for (a) CM, (b) CMT, (c) CMF, and (d) CMFT. Lattice parameters were calculated, using $a_c = a_{ortho}/\sqrt{2}$, $b_c = b_{ortho}/\sqrt{2}$ and $a_c = c_{ortho}/2$ for the orthorhombic (*Pnma*) structure, and $a_c = b_c = a_{tetra}/\sqrt{2}$ and $c_c = c_{tetra}/2$ for the tetragonal (*I*4/*mcm*) structure. For the cubic (*Pm*$\bar{3}$*m*) structure $a_c = b_c = c_c = a_{cubic}$.

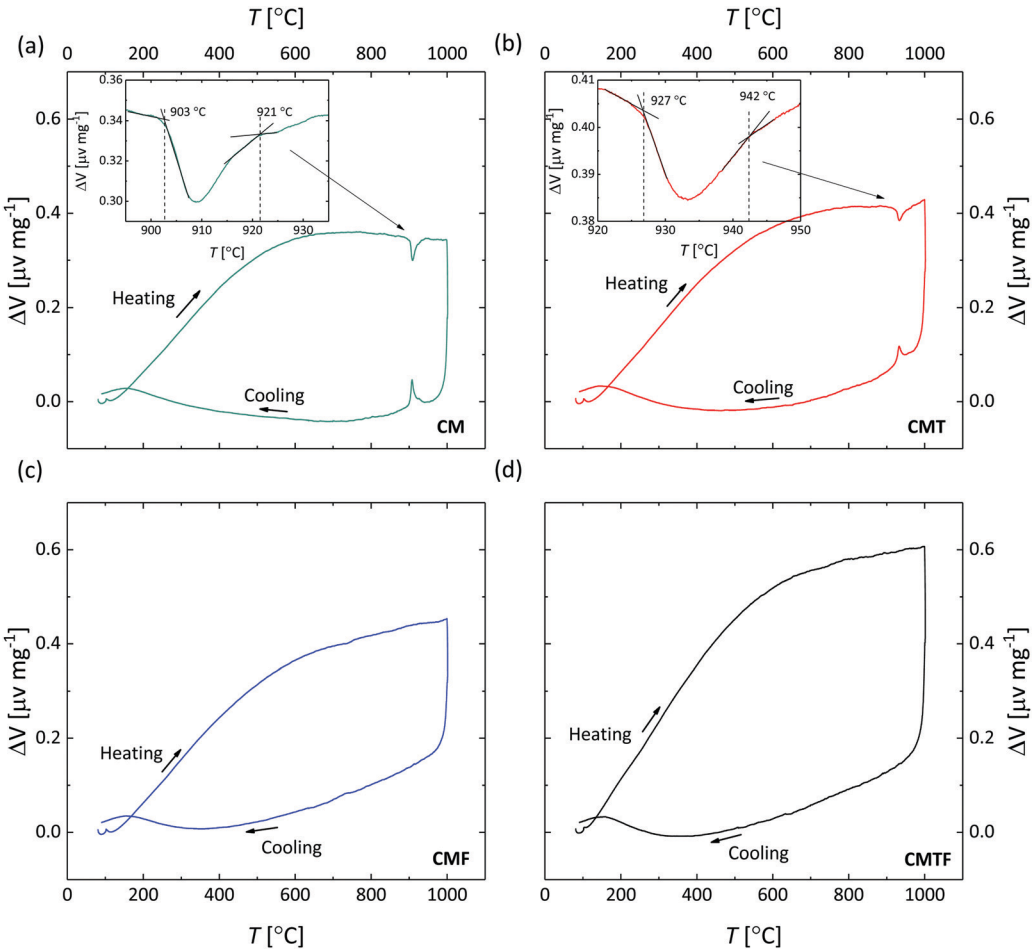

Fig. 3 DTA curves for (a) CM, (b) CMT, (c) CMF, and (d) CMTF recorded under heating and cooling in synthetic air. The insets in (a) and (b) show magnified regions around the endothermic phase transitions occurring upon heating in CM and CMT, respectively.

from tetragonal to cubic ($Pm\bar{3}m$) at 913 °C. In subsequent thermal analysis studies,[21,23] the two sequential peaks observed in this temperature region were assigned to these phase transitions. Pseudo-cubic lattice parameters obtained from Rietveld refinements of the HT-XRD patterns recorded for CM (with intervals of 25 °C) in this study are given in Fig. 2a. Our results reveal that CM remains orthorhombic up to 875 °C. Refinements of the patterns obtained in the range 900–950 °C yield a mixture of orthorhombic and tetragonal phases. Only at 975 °C a pure tetragonal phase, and at 1000 °C a pure cubic phase is obtained. Results from DTA carried out in this study as shown in Fig. 3a confirm the presence of two sequential endothermic phase transitions on heating of CM in air, albeit that the second peak is significantly less distinct than observed in some of the above-cited studies.[21–23] There are only small discrepancies between the onset temperatures found in this study (903 °C and 921 °C) and those reported by Taguchi *et al.*[22] (896 °C and 913 °C) and Rørmark *et al.*[21] (904 °C and 923 °C).

Lattice parameters from Rietveld refinements of the HT-XRD patterns for CMT are given in Fig. 2b. The DTA curve recorded for this material is shown in Fig. 3b, from which it is obvious that the endothermic phase transitions observed on heating of CM are shifted to slightly higher temperatures (927 °C and 942 °C) in CMT. The Rietveld refinements for CMT, however, do not give evidence for a phase transition in this material. The HT-XRD patterns can be indexed orthorhombic up to the maximum temperature of 1000 °C covered by the experiments (see Fig. 2b). The refinements of the HT-XRD patterns for CMF and CMTF (see Fig. 2c and d, respectively) show an orthorhombic → tetragonal → cubic sequence of transitions occurring upon heating of both materials, which is consistent with that found for parent CM by Taguchi *et al.*;[22] the indexing of the patterns is found compatible with space groups *Pnma*, *I*4/*mcm* and $Pm\bar{3}m$, respectively. The same sequence of phase transitions has been reported for $CaFe_xTi_{1-x}O_{3-\delta}$.[24,25] Structural parameters and reliability factors obtained from typical Rietveld refinements for every space group of CMF and CMTF are given in Tables S1 and S2 (ESI†), respectively. The DTA curves recorded for CMF and CMTF are shown in Fig. 3c and d, respectively. No peaks can be discerned, indicating that the structural transitions in both materials are continuous.

3.2 Oxygen nonstoichiometry

Although data of high-temperature neutron diffraction could resolve apparent ambiguities, the temperature-induced phase transitions as observed in CM, CMF and CMTF are believed to result from cooperative tilting of BO_6 octahedra, which is the

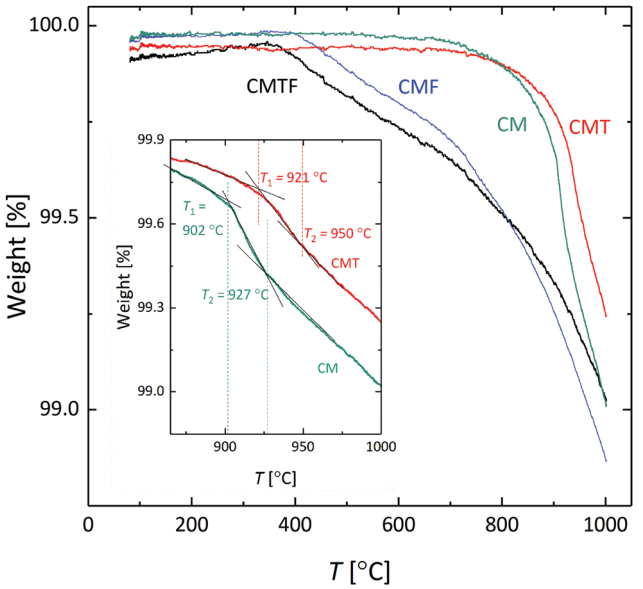

Fig. 4 TGA of CM, CMT, CMF and CMTF during heating and cooling in synthetic air at 10 °C min^{-1}. The inset shows a magnification of the temperature region where phase transitions occur in CM and CMT.

most commonly observed distortion in perovskite structures.[26,27] The orthorhombic *Pnma* structure, in Glazer's notation[28,29] denoted by $a^-a^-c^+$, is one of the most common perovskite variants with a three-tilt system.[26,27] With increasing temperature, materials with this structure lose their tilts *via* a series of transitions, ending up with the ideal cubic $Pm\bar{3}m$ structure, in which there are no tilts ($a^0a^0a^0$).[30] Several authors have discussed that the sequence of structural phase transitions in parent CM is influenced by the degree of oxygen nonstoichiometry exhibited by the material.[20,21] From the pO_2-T-δ phase diagram of CM published by Leonidova *et al.*[20] it may be inferred that the intermediate tetragonal $I4/mcm$ structure with tilt configuration $a^0a^0c^-$ is absent at ideal oxygen stoichiometry. Results of density functional theory (DFT) calculations indicate that the phase may appear as a result of ordering of oxygen vacancies.[30]

The temperature and oxygen partial pressure dependence of the oxygen nonstoichiometry of CM, CMT, CMF and CMTF in this work was studied by TGA. Fig. 4 shows the corresponding weight changes as a function of temperature during heating in synthetic air (pO_2 = 0.21 atm). The weight changes are found reversible on heating and cooling (not shown). Oxygen loss for CMF and CMTF starts around 350–400 °C, while for CM and CMT oxygen is not released below about 650 °C. The degree of oxygen nonstoichiometry at equal temperatures is notably more pronounced for the former two materials, which is ascribed to the presence of the more reducible iron cations.

The inset in Fig. 4 shows that the slope of the temperature dependence of the weight change in both CM and CMT changes slightly after the apparent phase transitions occurring in both materials. For CM, this observation is consistent with the phase diagram published by Leonidova *et al.*[20] The observed onset temperatures, 902 °C and 927 °C for CM and 921 °C and 950 °C for CMT, are in fair agreement with the corresponding results from DTA (see Fig. 3).

As shown by Leonidova *et al.*[20] and Rørmark *et al.*,[21] the phase transition temperatures in CM decrease with increasing oxygen deficiency. It is therefore postulated here that the lower transition temperatures observed for CMF and CMTF (*cf.* Fig. 2c and d, respectively) compared to those reported for CM by, *e.g.*, Taguchi *et al.*[22] might be related to the comparatively high oxygen deficiencies exhibited by the former two materials. This further suggests that the transition temperatures can be tuned by the degree of manganese substitution. Additional research is required to demonstrate our hypothesis.

The oxygen stoichiometry $(3-\delta)$ as a function of log (pO_2) for the different materials is presented in Fig. 5. The corresponding TGA measurements were performed to support analysis of data obtained from ECR measurements as will be discussed below. For the evaluation it was assumed that $\delta = 0$ at room temperature.

3.3 Electrical conductivity

Fig. 6 shows the temperature dependences of the electrical conductivity of the investigated materials in this study as a function of temperature at pO_2 = 0.21 atm. The conductivity of CM, CMF and CMTF show Arrhenius behaviour with activation energies in the range 80–92 kJ mol^{-1}. For CMT, a change in activation energy is apparent at about 875 °C.

Electrical conductivity in undoped CM is due to the formation of small polarons, which migrate *via* thermally activated hopping.[24,25] Charge disproportionation, involving the transfer of an electron between adjacent Mn^{4+} ions,

$$2Mn_{Mn}^{\times} = Mn_{Mn}' + Mn_{Mn}^{\bullet} \quad (8)$$

leads to the formation of localized electrons $Mn^{3+}(Mn_{Mn}')$ and electron holes Mn^{5+} $(Mn_{Mn}^{\bullet})$ that are trapped by local lattice distortions due to electron–phonon coupling: these are the n- and p-type small polarons, respectively. Throughout this paper standard Kröger–Vink notation is used to describe defect chemical reactions. The negative sign of the Seebeck coefficient confirms that the n-type polarons are the dominant charge carriers in CM.[20,31] The p-type polaronic charge carriers in CM appear to be effectively immobile.[20] The electrical conductivity in CM is thus expected to obey: $\sigma \propto \mu[Mn_{Mn}'][Mn_{Mn}^{\times}]$, the latter denoting the product of the number of charge carriers and the number of sites to which they can hop. Since variations in $[Mn_{Mn}^{\times}]$ are very small,[32] the conductivity is thus essentially governed by the concentration of Mn^{3+} cations $([Mn_{Mn}'])$. In addition to reaction (8), their concentration is affected by the exchange of oxygen between the gas phase and the oxide,

$$O_2(g) + 2V_O^{\bullet\bullet} + 4Mn_{Mn}' = 2O_O^{\times} + 4Mn_{Mn}^{\times} \quad (9)$$

and by aliovalent doping. Charge neutrality requirements predict that acceptor doping, *e.g.*, Fe^{3+} substituted for Mn^{4+} (Fe_{Mn}') will lower the electrical conductivity, which is accord with the observation that the electrical conductivity decreases on going from CM to CMF (Fig. 6). Such an explanation is also consistent

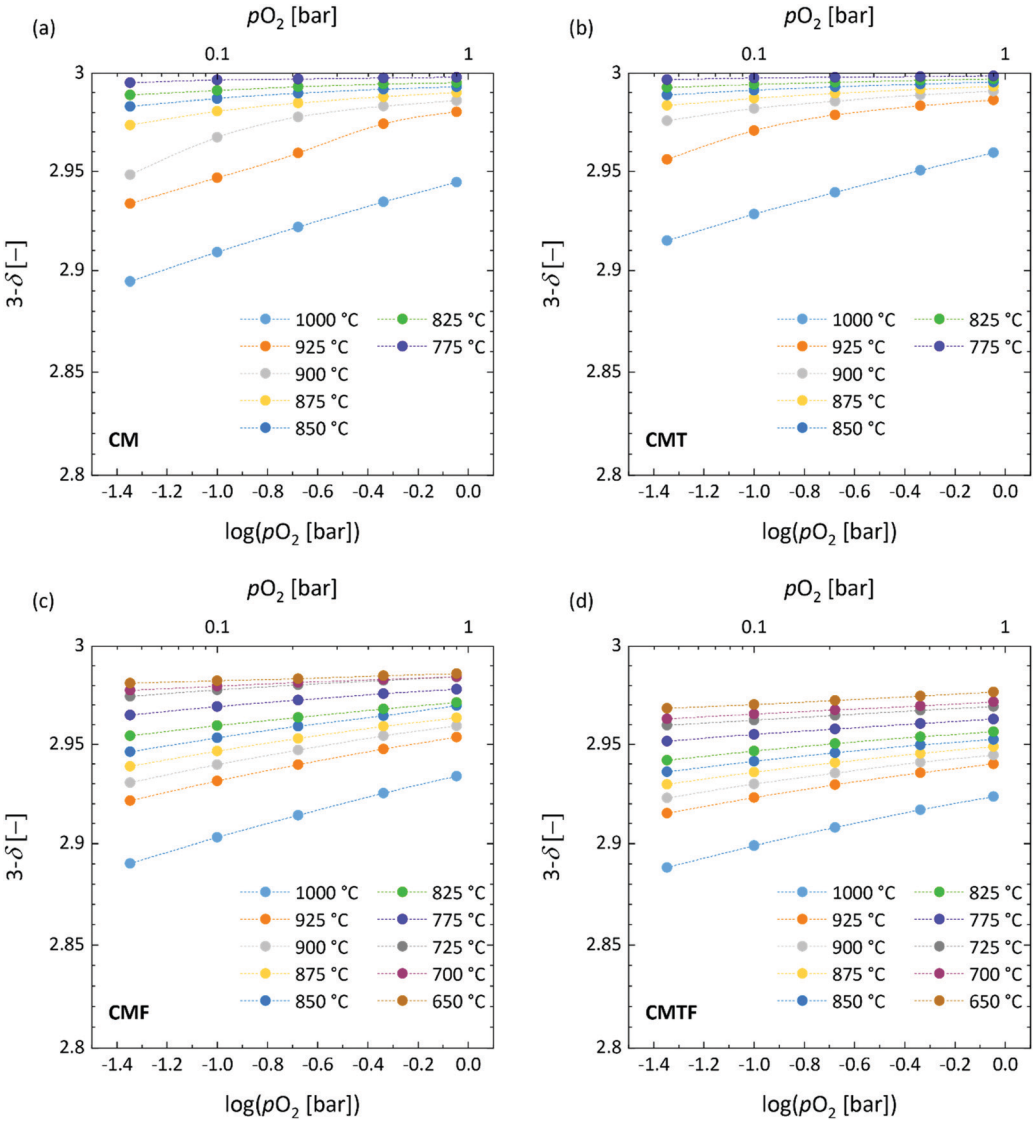

Fig. 5 Oxygen stoichiometry (3 − δ) at different temperatures for (a) CM, (b) CMT, (c) CMF and (d) CMTF calculated from data of TGA. Dashed lines are drawn to guide the eye.

with the increase in electrical conductivity observed upon donor doping of CM with Nb^{5+}.[33] It is further seen from Fig. 6 that the electrical conductivity of CM drops almost half an order of magnitude after the isovalent substitution of Mn^{4+} with Ti^{4+} ions, suggesting that it is the mobility of the n-type small polarons that is highly affected by the titanium substitution. A detailed study, however, is required to substantiate this conclusion and to provide further insights into the mechanism of electrical conduction in these solids. Additional investigations are also required to clarify the origin of the change in activation energy of the electrical conductivity found for CMT at about 875 °C (Fig. 6).

3.4 Electrical conductivity relaxation

The oxygen transport properties of CM, CMT, CMF and CMTF were evaluated by ECR experiments. Normalized conductivity curves acquired from 925 to 650 °C after a pO_2 step change from 0.215 to 0.146 atm for CMT are shown in Fig. 7. Excellent reproducibility was found during heating and cooling experiments. Similar results were obtained for the other compositions. In general, faster re-equilibration times after a pO_2 step change are obtained with increase of temperature, although it should be noted that in the specific case of CMT (as can be inferred from Fig. 7) and that of CM (not shown) the re-equilibration times at the highest temperatures are observed to increase again with further increase of temperature.

Measurement accuracy. A typical fit and associated error colour map obtained from fitting of the data of a single relaxation experiment are shown in Fig. S2 (ESI†). Analysis of experimental data allows simultaneous determination of D_{chem} and k_{chem} provided that both processes contribute in a quantifiable manner to the overall relaxation process. The latter is constrained by the accuracy of measurements, *e.g.*, the noise of data, but also by the extent to which the re-equilibration after a pO_2 step change is

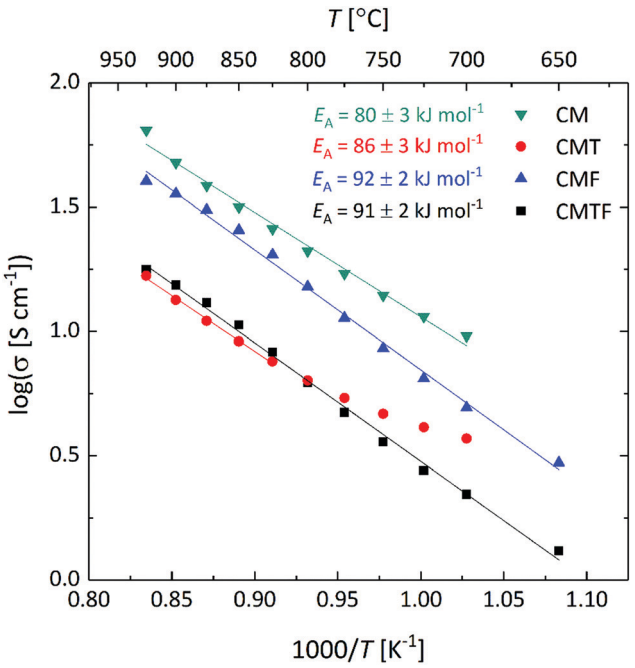

Fig. 6 Total electrical conductivity as a function of temperature measured at pO_2 = 0.21 atm.

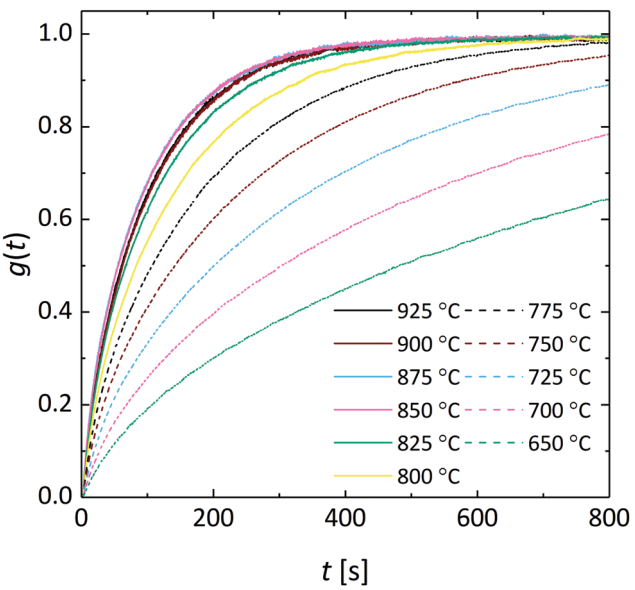

Fig. 7 Normalized conductivity curves for CMT. Data are acquired from 925 to 650 °C, with 25 °C intervals, after a pO_2 step change from 0.215 to 0.146 atm.

determined by diffusion and by surface exchange. A useful quantity in this respect is $b_z/L_c = b_z k_{chem}/D_{chem}$ (*cf.* eqn (4), noting that $b_z \ll b_x, b_y$), which can be identified with the Biot number (Bi) commonly used in analysis of mass transport, and which parameter represents the ratio between two characteristic times: b_z^2/D_{chem} for diffusion and b_z/k_{chem} for surface exchange. A Biot plot for the data obtained in this study is given in Fig. 8, showing that for given thicknesses and conditions (see the Experimental section)

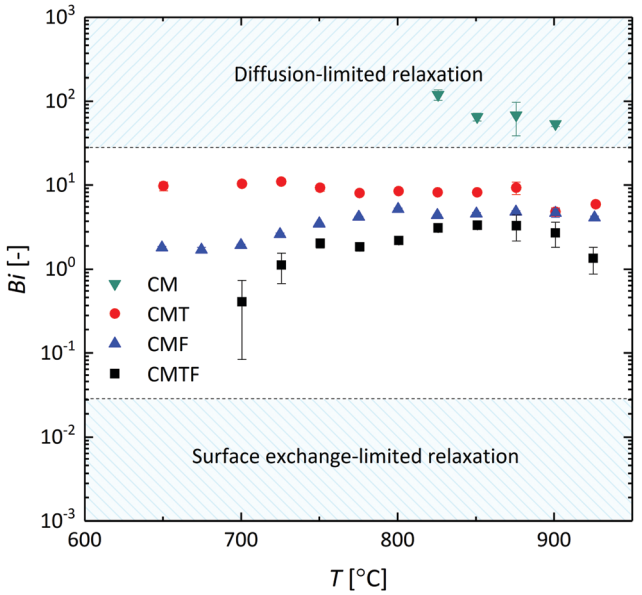

Fig. 8 Biot number (Bi) as a function of temperature. Error bars indicate the standard error calculated based on averaging at least three experiments per temperature. Following Den Otter *et al.*[18] the mixed-controlled region is found for 0.03 ≤ Bi ≤ 30.

oxygen transport in CMT, CMF and CMTF over the entire range in temperature is in the mixed controlled region (0.03 ≤ Bi ≤ 30),[7] whereas that of CM is in the diffusion-controlled region. Over a large range in temperature it was not possible to extract values of k_{chem} for CM from the data of experiments.

Chemical diffusion and surface exchange coefficients. Arrhenius plots of D_{chem} and k_{chem} derived from the data of ECR measurements on CM, CMT, CMF and CMTF are shown in Fig. 9. A reasonable to good agreement of the values extracted from data of oxidation and reduction runs is obtained, suggesting that at given experimental conditions the constancy of D_{chem} and k_{chem} over the applied pO_2 step change as assumed in the fitting procedure is satisfied accordingly.[18] Fig. 9 shows that the Arrhenius plots of D_{chem} and k_{chem} for all four compositions studied are subject to significant curvature. The curvature of the plots appears to be highly similar for both parameters, which holds for CMT, CMF and CMTF, suggesting that for each of these materials D_{chem} and k_{chem} are strongly correlated. Other authors have arrived at similar conclusions on the basis of studies on different materials. For example, see ref. 34, 35, 36 and 37. A similar statement cannot be made for CM since, as was mentioned above, accurate values for k_{chem} for CM could not be obtained from the fitting procedure.

Oxygen self-diffusion and vacancy diffusion coefficients. To further analyse the data, the oxygen self-diffusion coefficients, D_s, and the oxygen vacancy diffusion coefficients, D_V, for CM, CMT, CMF and CMTF were evaluated from the measured values of D_{chem}, using the relationships

$$D_{chem} = \gamma_O D_S \quad (10)$$

$$D_{chem} = \gamma_V D_V \quad (11)$$

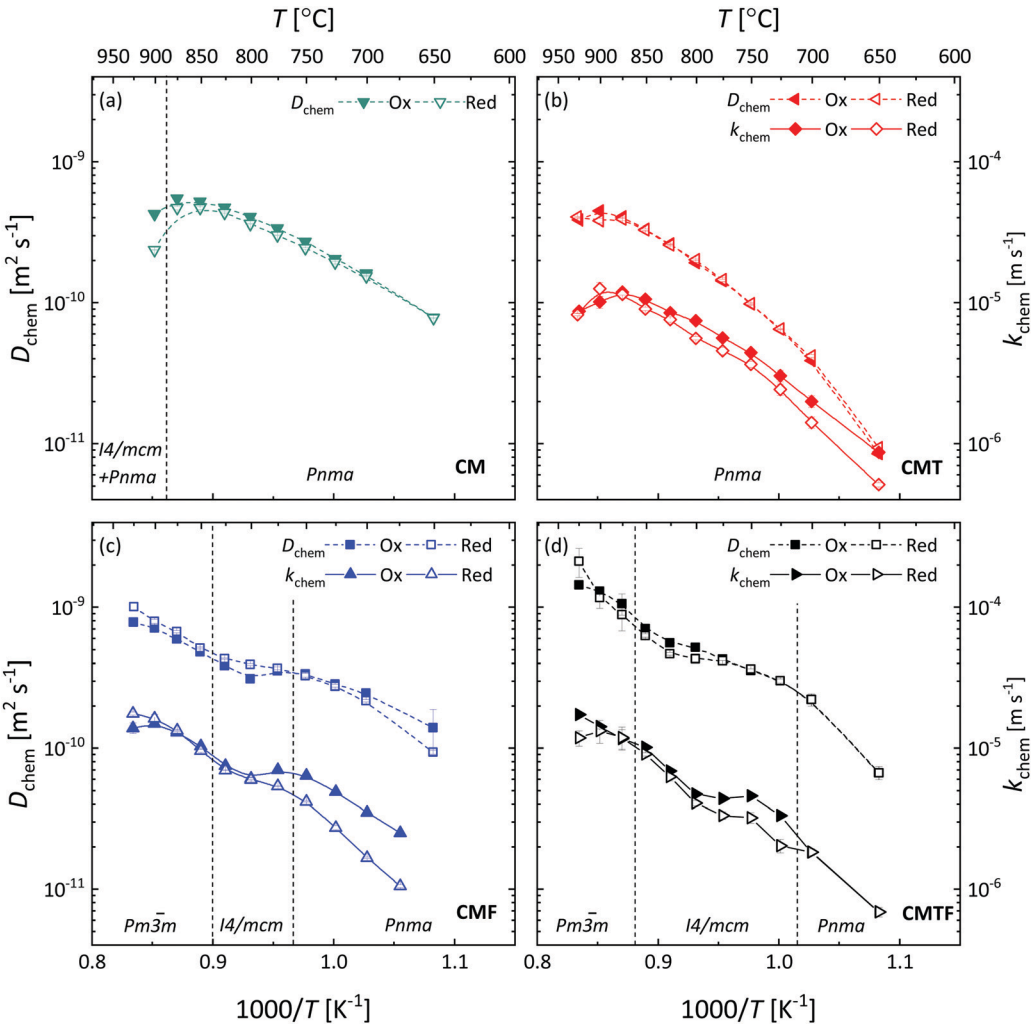

Fig. 9 Inverse temperature dependence of the chemical diffusion coefficient (D_{chem}) and the surface exchange coefficient (k_{chem}) for (a) CM, (b) CMT, (c) CMF, and (d) CMTF. Dashed lines serve as a guide to the eye. The filled and open symbols represent the data of oxidation and reduction step changes, respectively. The structures occurring in the different temperature regions are designated by their space groups. The vertical dashed lines denote by approximation the temperatures at which the phase transitions occur.

where γ_O and γ_V are the thermodynamic factors,[8]

$$\gamma_O = \frac{1}{2}\frac{\partial \ln(pO_2)}{\partial \ln(3-\delta)} = \frac{(3-\delta)}{2}\frac{\partial \ln(pO_2)}{\partial(3-\delta)} \quad (12)$$

$$\gamma_V = -\frac{1}{2}\frac{\partial \ln(pO_2)}{\partial \ln(\delta)} = -\frac{\delta}{2}\frac{\partial \ln(pO_2)}{\partial(\delta)} = \frac{\delta}{2}\frac{\partial \ln(pO_2)}{\partial(3-\delta)} \quad (13)$$

which can be derived from corresponding data of the oxygen nonstoichiometry for each of the compositions (Fig. 5). Strictly speaking, eqn (10) and (11) hold for materials with predominant electronic conductivity.[8] Corresponding results for D_S and D_V for all four compositions are given in Fig. 10 and 11, respectively. The results reveal that for CMT (Fig. 10b and 11b) both parameters show Arrhenius behaviour over the entire range in temperature covered by the experiments. For CM (Fig. 10a and 11a), the linear behaviour extends up to 875 °C, above which temperature the material transforms partially from orthorhombic (*Pnma*) to a mixture of orthorhombic (*Pnma*) and tetragonal (*I4/mcm*) phases. The high values observed for the average activation energies of D_S, 240 ± 19 kJ mol^{-1} and 275 ± 15 kJ mol^{-1} for CM and CMT, respectively, confirm that there are very few oxygen vacancies in both materials. The latter is reflected in the much lower activation energies found for D_V of both compositions, 75 ± 17 kJ mol^{-1} and 113 ± 16 kJ mol^{-1} for CM and CMT, respectively.

The temperature dependences of D_S (Fig. 10c and d, respectively) and D_V (Fig. 11c and d, respectively) for CMF and CMTF show significant departures from linear Arrhenius behaviour. For both compositions, the log(D_S) *vs.* 1/T and log(D_V) *vs.* 1/T plots show a reverse S-shape, *i.e.*, the log(D_S) and log(D_V) values levelling off in the intermediate temperature region, while increasing again at higher temperatures. The different temperature regions can be linked to the orthorhombic → tetragonal → cubic transformations occurring in both materials.

Overall, the results in this study suggest that oxygen transport in the tetragonal *I4/mcm* phase, which occurs in CM, CMF and CMTF, and possibly also in CMT at higher temperatures than

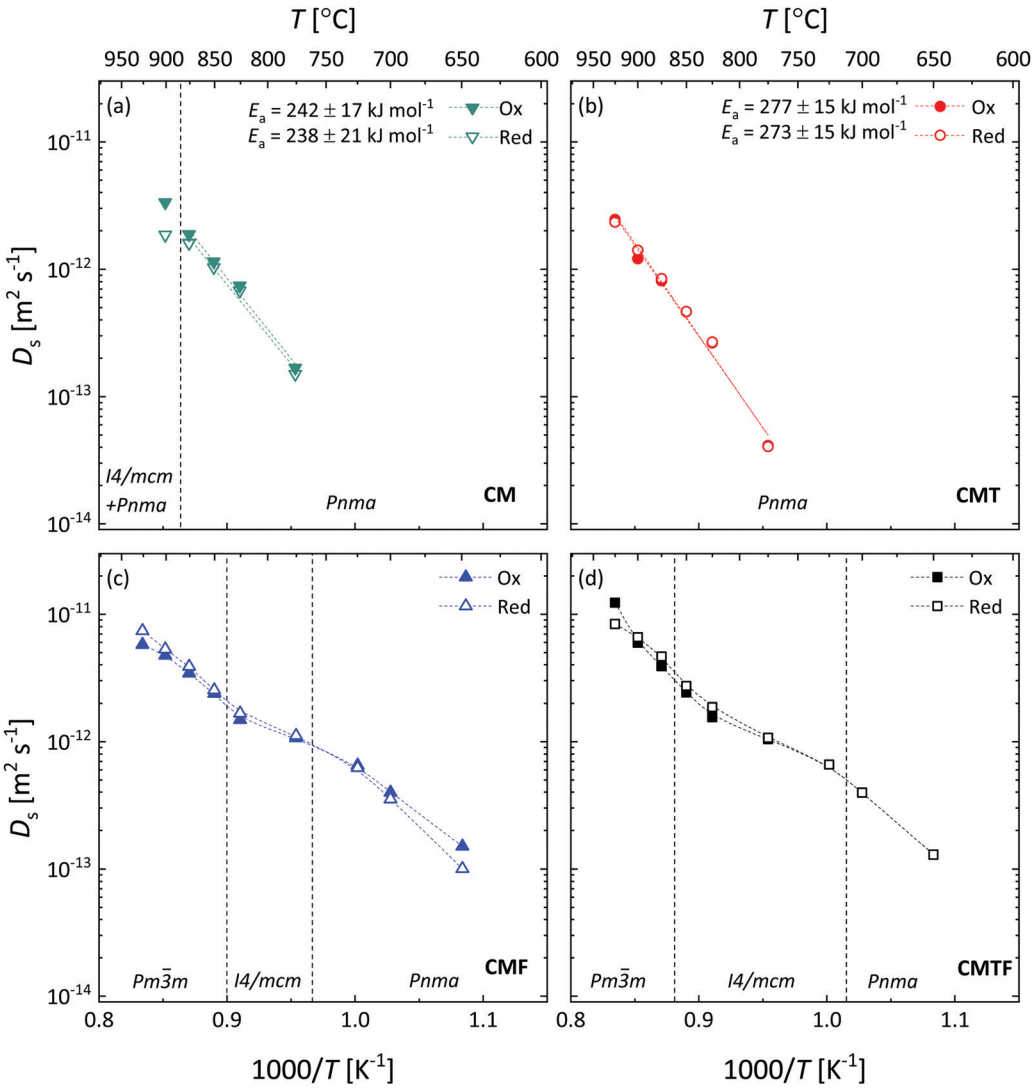

Fig. 10 Inverse temperature dependence of the oxygen self-diffusion coefficient (D_s) for (a) CM, (b) CMT, (c) CMF, and (d) CMTF. Dashed lines serve as a guide to the eye. The filled and open symbols represent the data of oxidation and reduction step changes, respectively. The structures occurring in the different temperature regions are designated by their space groups. The vertical dashed lines denote by approximation the temperatures at which the phase transitions occur.

those covered by the present investigations, is reduced, *e.g.*, by (partial) ordering of oxygen vacancies. The latter would be consistent with the results of recent DFT calculations on the parent phase CM by Klarbring and Simak,[30] in which the authors show that it is unlikely that the tetragonal phase appears as a result of a purely displacive mechanism, but rather may appear as a result of an ordering of oxygen vacancies. Further structural investigations using high-temperature neutron diffraction would be required to confirm these findings.

4. Conclusions

The present study reveals that $CaMnO_{3-\delta}$ (CM) transforms from orthorhombic to a mixture of orthorhombic and tetragonal phases at temperatures exceeding ~875 °C. The Rietveld refinements yield formation of a pure tetragonal phase at 975 °C and of a pure cubic phase at 1000 °C. It is further found that in the temperature range 600–1000 °C $CaMn_{0.85}Fe_{0.15}O_{3-\delta}$ (CMF) and $CaMn_{0.725}Ti_{0.125}Fe_{0.15}O_{3-\delta}$ (CMTF) undergo a sequence of phase transitions from orthorhombic to tetragonal to cubic. $CaMn_{0.875}Ti_{0.125}O_{3-\delta}$ (CMT) is found to remain orthorhombic up to the highest temperatures covered by the HT-XRD experiments. The small polaron hopping conductivity of CM is reduced by partial manganese substitution with iron and/or titanium. Distinct departures of the temperature dependences of the oxygen self-diffusion and oxygen vacancy diffusion coefficients for CM, CMF and CMFT from Arrhenius-type of behaviour are interpreted to reflect reduced oxygen transport in the tetragonal phases occurring in these materials. The latter is consistent with recent results of DFT calculations on the parent phase CM showing that the tetragonal

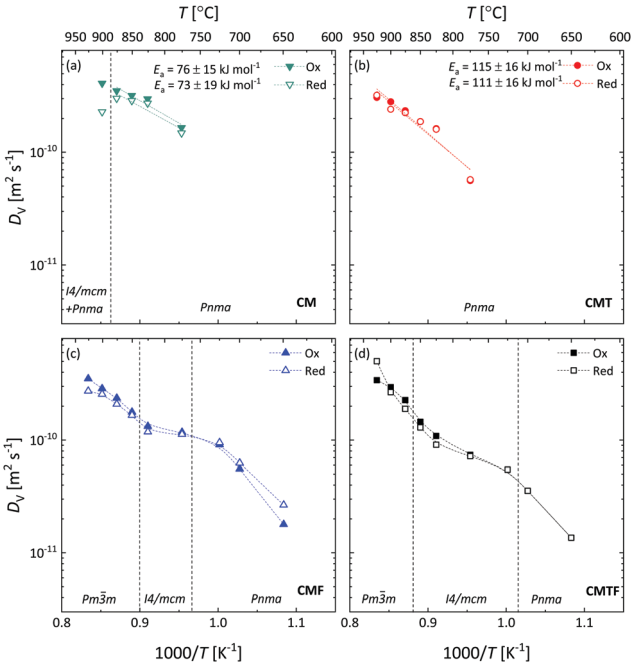

Fig. 11 Inverse temperature dependence of the oxygen vacancy coefficient (D_V) for (a) CM, (b) CMT, (c) CMF, and (d) CMTF. Dashed lines serve as a guide to the eye. The filled and open symbols represent the data of oxidation and reduction step changes, respectively. The structures occurring in the different temperature regions are designated by their space groups. The vertical dashed lines denote by approximation the temperatures at which the phase transitions occur.

phase may appear as a result of an ordering of oxygen vacancies.

Conflicts of interest

There are no conflicts to declare.

Acknowledgements

Financial support from the EU FP7 research project GREEN-CC (GA 608524) is gratefully acknowledged. The performed work was part of the BIGCLC Phase III project supported by the Research Council of Norway (id 224866 and id 193816). J. S. acknowledges financial support by the Chinese Scholarship Council (CSC 201406340102). The authors would like to thank Youngsung Lee and Hiroshige Matsumoto of the Kyushu University (Japan) for assistance with the HT-XRD measurements.

References

1 P. Wang, N. Means, D. Shekhawat, D. Berry and M. Massoudi, *Energies*, 2015, **8**, 10605–10635.
2 A. Thursfield, A. Murugan, R. Franca and I. S. Metcalfe, *Energy Environ. Sci.*, 2012, **5**, 7421–7459.
3 J. Hu, V. V. Galvita, H. Poelman and G. B. Marin, *Materials*, 2018, **11**, 1187.
4 L. Zeng, Z. Cheng, J. A. Fan, L.-S. Fan and J. Gong, *Nat. Rev. Chem.*, 2018, **2**, 349–364.
5 H. Yang, Z. Xu, M. Fan, R. Gupta, R. B. Slimane, A. E. Bland and I. Wright, *J. Environ. Sci.*, 2008, **20**, 14–27.
6 M. E. Boot-Handford, J. C. Abanades, E. J. Anthony, M. J. Blunt, S. Brandani, N. Mac Dowell, J. R. Fernandez, M. C. Ferrari, R. Gross, J. P. Hallett, R. S. Haszeldine, P. Heptonstall, A. Lyngfelt, Z. Makuch, E. Mangano, R. T. J. Porter, M. Pourkashanian, G. T. Rochelle, N. Shah, J. G. Yao and P. S. Fennell, *Energy Environ. Sci.*, 2014, **7**, 130–189.
7 J. Sunarso, S. Baumann, J. M. Serra, W. A. Meulenberg, S. Liu, Y. S. Lin and J. C. D. da Costa, *J. Membr. Sci.*, 2008, **320**, 13–41.
8 H. J. M. Bouwmeester and A. J. Burggraaf, in *The CRC Handbook of Solid State Electrochemistry*, ed. P. J. Gellings and H. J. M. Bouwmeester, CRC Press, Boca Raton, 1996, p. 481, 1997.
9 X. Dong, W. Jin, N. Xu and K. Li, *Chem. Commun.*, 2011, **47**, 10886–10902.
10 W. Deibert, M. E. Ivanova, S. Baumann, O. Guillon and W. A. Meulenberg, *J. Membr. Sci.*, 2017, **543**, 79–97.
11 P. Hallberg, D. Jing, M. Rydén, T. Mattisson and A. Lyngfelt, *Energy Fuels*, 2013, **27**, 1473–1481.
12 H. Leion, Y. Larring, E. Bakken, R. Bredesen, T. Mattisson and A. Lyngfelt, *Energy Fuels*, 2009, **23**, 5276–5283.
13 S. Sundqvist, H. Leion, M. Rydén, A. Lyngfelt and T. Mattisson, *Energy Technol.*, 2013, **1**, 338–344.
14 V. Thoréton, M. Pishahang, T. Mokkelbost, K. Wiik and Y. Larring, *Energy Technol.*, 2017, **5**, 1579–1587.
15 W. Xing, M.-L. Fontaine, Z. Li, J. M. Polfus, Y. Larring, C. Denonville, E. Nonnet, A. Stevenson, P. P. Henriksen and R. Bredesen, *J. Membr. Sci.*, 2018, **548**, 372–379.
16 N. M. Mazur, *Microstructural design of $CaMnO_3$ and its thermoelectric properties, Master thesis,* Norwegian University of Science and Technology (NTNU), Trondheim, Norway, 2015.
17 J. Rodríguez-Carvajal, *Phys. B*, 1993, **192**, 55–69.
18 M. W. den Otter, H. J. M. Bouwmeester, B. A. Boukamp and H. Verweij, *J. Electrochem. Soc.*, 2001, **148**, J1–J6.
19 G. Watterud, PhD Thesis, Norwegian University of Science and Technology (NTNU), Norway, 2005.
20 E. I. Leonidova, I. A. Leonidov, M. V. Patrakeev and V. L. Kozhevnikov, *J. Solid State Electrochem.*, 2011, **15**, 1071–1075.
21 L. Rørmark, K. Wiik, S. Stolen and T. Grande, *J. Mater. Chem.*, 2002, **12**, 1058–1067.
22 H. Taguchi, M. Nagao, T. Sato and M. Shimada, *J. Solid State Chem.*, 1989, **78**, 312–315.
23 P. Thiel, S. Populoh, S. Yoon and A. Weidenkaff, *J. Solid State Chem.*, 2015, **229**, 62–67.
24 A. I. Becerro, S. A. T. Redfern, M. A. Carpenter, K. S. Knight and F. Seifert, *J. Solid State Chem.*, 2002, **167**, 459–471.
25 S. A. T. Redfern, *J. Phys.: Condens. Matter*, 1996, **8**, 8267–8275.
26 C. J. Howard and H. T. Stokes, *Acta Crystallogr., Sect. B: Struct. Crystallogr. Cryst. Chem.*, 1998, **54**, 782–789.
27 C. J. Howard and H. T. Stokes, *Acta Crystallogr., Sect. A: Found. Crystallogr.*, 2005, **61**, 93–111.

28 A. M. Glazer, *Acta Crystallogr., Sect. B: Struct. Crystallogr. Cryst. Chem.*, 1972, **28**, 3384–3392.
29 A. M. Glazer, *Acta Crystallogr., Sect. A: Found. Crystallogr.*, 1975, **31**, 756–762.
30 J. Klarbring and S. I. Simak, *Phys. Rev. B*, 2018, **97**, 024108.
31 M. Schrade, R. Kabir, S. Li, T. Norby and T. G. Finstad, *J. Appl. Phys.*, 2014, **115**, 103705.
32 E. I. Goldyreva, I. A. Leonidov, M. V. Patrakeev and V. L. Kozhevnikov, *J. Solid State Electrochem.*, 2012, **16**, 1187–1191.
33 L. Bocher, M. H. Aguirre, R. Robert, D. Logvinovich, S. Bakardjieva, J. Hejtmanek and A. Weidenkaff, *Acta Mater.*, 2009, **57**, 5667–5680.
34 J. A. Kilner, R. A. De Souza and I. C. Fullarton, *Solid State Ionics*, 1996, **86–88**, 703–709.
35 R. A. De Souza and J. A. Kilner, *Solid State Ionics*, 1999, **126**, 153–161.
36 L. M. van der Haar, M. W. den Otter, M. Morskate, H. J. M. Bouwmeester and H. Verweij, *J. Electrochem. Soc.*, 2002, **149**, J41–J46.
37 S. Saher, M. Meffert, H. Störmer, D. Gerthsen and H. J. M. Bouwmeester, *J. Mater. Chem. A*, 2017, **5**, 4982–4990.